Diamond & Related Materials 126 (2022) 109059

Contents lists available at ScienceDirect

Diamond & Related Materials

journal homepage: www.elsevier.com/locate/diamond

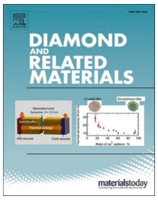

Improved microwave absorption traits of coconut shells-derived activated carbon

Wahyu Widanarto [a,*], Siska Irma Budianti [a], Sib Krishna Ghoshal [b], Candra Kurniawan [c], Erfan Handoko [d], Mudrik Alaydrus [e]

[a] Department of Physics, FMIPA, Universitas Jenderal Soedirman, Jl. dr. Soeparno 61, Purwokerto 53123, Indonesia
[b] Department of Physics and Laser Centre, AMORG, Faculty of Science, Universiti Teknologi Malaysia, Johor Bahru, Skudai 81310, Malaysia
[c] Research Center for Physics, Indonesian Institute of Sciences (LIPI), Puspiptek Office Area, South Tangerang, Banten 15314, Indonesia
[d] Department of Physics, Universitas Negeri Jakarta, Jl. Rawamangun Muka, Jakarta 13220, Indonesia
[e] Department of Electrical Engineering, Universitas Mercu Buana, Jl. Meruya Selatan, Jakarta 11650, Indonesia

ARTICLE INFO

Keywords:
Activated carbon
Milling
Fullerene-C_{70}
Permeability
Permittivity
MW reflection loss

ABSTRACT

Novel multi-functional materials with very high microwave (MW) absorbance in the X-band became demanding for varied high-sensitive electronic applications. To meet this goal, a new type of activated carbon sample containing fullerene-C_{70} was derived from coconut shells using the combined physical activation and milling process for the first time. The effects of various milling times (50, 75, and 100 min) on the structure, morphology, and MW reflection traits of these samples were examined. The crystalline phase of the activated fullerene-C_{70} was found to alter from cubic to rhombohedral structure at the milling time of 100, displaying a specific surface area of 946.499 m^2/g and mean pore diameter of 3.42 nm. It was shown that by tuning the surface area and fullerene contents in the sample, the MW reflection loss of such activated carbon can be controlled. It is established that fullerene-C_{70} derived from the proposed activated carbon may be useful to produce low-cost and efficient MW absorption materials needed for diverse electronic devices with reduced electromagnetic interference.

1. Introduction

With the development of microwave (MW)-based electronic technology electromagnetic wave pollution became a serious environmental concern, greatly affecting human health and normal operations of electronic devices. To mitigate these problems, electromagnetic wave absorbing materials have intensively been researched in recent years. Coating the target with an efficient electromagnetic wave absorbing material is a method to reduce the intensity of the reflected or transmitted electromagnetic waves [1–7]. This method utilizes the absorption or dispersion of electromagnetic energy in the medium between the electromagnetic wave source and the protected target. It imparts the electromagnetic wave absorbing materials the ability to absorb unwanted electromagnetic waves and stability against temperature and oxidation. In addition, they are easy to manufacture, flexible and affordable to become one of the *high-tech* essential materials.

Extensive research revealed that the performance of the carbon nanomaterials and their composites like graphene, carbon spheres, carbon nanotubes are great potential in attenuating the electromagnetic waves [8–12]. Activated carbon is a carbon source that can be obtained by activating carbon physically or chemically. The surface morphology of the porous activated carbon is one of the unique characteristics that can be used in many applications such as dye absorbers, oil purification, supercapacitor electrodes, secondary battery electrodes, and others [8,13–16]. Some recent studies revealed that porous carbon nanostructures are advantageous to enhance their electromagnetic wave absorption characteristics [17,18]. Essentially, the magnetic components insertion inside the carbon materials [19,20] and hollow carbon spheres [21,22] are the effective strategies to appreciably improve the electromagnetic radiation absorption performance of the resultant products. However, to revalidate such claims more systematic investigations on new types of activated carbon nanomaterials are needed.

Considering the immense applied potential of the activated carbon materials, some activated carbon was derived from the coconut shell using the milling technique to achieve their improved MW absorption properties in the X-band. The milling times were varied to modify the structures, morphologies, and electromagnetic radiation absorption attributes of the proposed activated carbon enclosing fullerene-C_{70}. A

---

* Corresponding author.
E-mail address: wahyu.widanarto@unsoed.ac.id (W. Widanarto).

https://doi.org/10.1016/j.diamond.2022.109059
Received 11 November 2021; Received in revised form 8 April 2022; Accepted 19 April 2022
Available online 25 April 2022

porous surface of the activated carbon with a very small volume was used to warp electromagnetic waves so that the internal surface reflections in the volume occurred, thus improving the heat dissipation quality of the electromagnetic energy. The as-prepared activated carbon samples were characterized to determine their milling time-dependent surface morphology, structure, specific surface area, porosity, and MW absorbance (in terms of reflection loss values) in the X-band.

2. Experimental

2.1. Preparation of activated carbon from coconut shells

Carbon was made via the carbonization process wherein coconut shells were burnt at 80 °C for an hour under oxygen-deficient conditions to eliminate the organic materials present in the shells. The loss of organic materials triggered the formation or opening of the carbon pores. Then, the burnt coconut shell-derived carbon was physically activated. Intense heat and water vapor enabled the severing of the carbon chains from the organic compounds. The heating as the physical activation process was intended to remove the impurities and impure hydrocarbons from the activated carbon. Next, the resultant carbon was heated in the temperature range of 800–900 °C followed by the water vapor streaming. The water vapor reacted with carbon, thus releasing carbon monoxide, carbon dioxide, and hydrogen. Thereafter, the activated carbon was pulverized using a Mill Shaker at different milling times of 50, 75, and 100 min to obtain the particles' sizes in the micrometer range. The extracted activated carbon powders were labeled as C-50, C-75, and C-100 according to various milling times. A small amount of activated carbon was bound utilizing resin to form a rectangular shape steady with the WR90 sample holder for measuring the reflection loss (R_L).

2.2. Characterizations

The morphology and microstructure of the prepared samples (C-50, C-75, and C-100) were examined using the scanning electron microscope (SEM, Hitachi SU 3500). The crystal structures and phases of the samples were measured using a SmartLab (3 kW) X-ray diffractometer equipped with the Cu-Kα line of wavelength (λ) ≈ 0.1541874 nm. The Surface Area Analyzer (SAA Quantachrome Instrument Version 11.03) was used to determine the specific surface area and pore diameter of the samples. The scattering characteristics (S) of the specimens were measured using a vector network analyzer (VNA) from Keysight (PNA-L N5232A). The MW absorbance values of the samples were calculated to get the components of S (S_{11}, S_{12}, S_{21}, and S_{22}). The values of S_{11} and S_{21} specify the coefficients of reflection (Γ) and transmission (T), respectively. The recorded values of S_{22} and S_{12} were ignored due to their corresponding similarity with S_{11} and S_{21}. Following the method of Nicholson-Ross-Weir (NRW), the relative complex permeability ($\mu_r = \mu' - j\mu''$) and permittivity ($\varepsilon_r = \varepsilon' - j\varepsilon''$) values of 4 mm thick samples were calculated using:

$$\mu_r = \frac{1+\Gamma}{\Lambda(1-\Gamma)\sqrt{\frac{1}{\lambda_0^2}-\frac{1}{\lambda_c^2}}} \tag{1}$$

$$\frac{1}{\Lambda^2} = -\left[\frac{1}{2\pi d}ln\left(\frac{1}{T}\right)\right]^2 \tag{2}$$

$$\varepsilon_r = \frac{\lambda_0^2}{\mu_r}\left(\frac{1}{\lambda_c^2} - \left[\frac{1}{2\pi d}ln\left(\frac{1}{T}\right)\right]^2\right) \tag{3}$$

where λ_0 is the wavelength in vacuum, λ_c is the cut-off wavelength, c is the speed of light, and d is the thickness of the sample. Meanwhile, the MW absorption properties of the samples were obtained from the calculated reflection loss (R_L) values based on the transmission/reflection line theory [7,23–26] given by:

$$R_L = 20log\left|\frac{Z_{in}-1}{Z_{in}+1}\right| \tag{4}$$

$$Z_{in} = \sqrt{\frac{\mu_r}{\varepsilon_r}}\tanh\left[-j\frac{2\pi fd}{c}\sqrt{\mu_r\varepsilon_r}\right] \tag{5}$$

where Z_{in} is the input impedance of the material and f is the MW frequency.

3. Results and discussion

3.1. Morphology of the activated carbon

Fig. 1 shows the SEM micrographs of the activated carbons that are pulverized at different milling times, which consisted of irregular microstructures. Interestingly, the formation of carbon particles with intergranular pores provided a large specific surface area that is suitable for strong interaction with the externally applied electromagnetic radiation. Together, these pores strongly favored the MW entrapment and its random dispersion in all directions facilitated by the finer particles in the pores, thereby improving the MW absorption traits of the proposed activated carbon specimen. In addition, several smaller particles were merged to form bigger particles through surface free energy minimization, indicating their thermodynamic stable state. Indeed, the growth and nucleation became more prominent in the C-100 specimen, leading to a significant difference in its reflectivity.

3.2. Structures and phase of the activated carbon

Fig. 2 displays the X-ray diffraction (XRD) patterns of all the milled samples. The XRD peaks of C-50 sample were matched to the cubic carbon (C – ICDD: 00-006-0675) with crystallographic parameters of $a = b = c = 0.35667$ nm and α = β = γ = 90°. Similar observations were made for C-75 and C-100 samples wherein the Bragg's peaks were dominated by the cubic carbon lattice (C – ICDD: 00-006-0675). Sample grown at the milling times of 100 min (C-100) consisted of fullerene-C_{70} carbon phase (C- ICDD 00-048-1449), showing intense XRD peak at 2θ = 23.90° with crystallographic parameters of $a = b = 0.98095$ nm, $c = 2.70220$ nm, and α = β = 90°, γ = 120°. It is known that fullerene-C_{70} enclosing seventy carbon atoms has a spherical caged structure made of 25 hexagons and 12 pentagons connected by single and double covalent bonds. Due to this unique structure of fullerenes, strong internal reflections occur in the spherical cage, thus enabling it a gifted MW absorber. Earlier studies indicated that fullerene being one of the efficient reinforcing materials can be greatly effective in absorbing MW radiation [27]. In addition, it was claimed that the graphite – fullerene composites can exhibit excellent MW absorption performance compared to pure graphite [28] which needs further validation.

3.3. Specific surface area and pore diameter of the activated carbon

Fig. 3 illustrates a multi-point isothermal BET plot of the activated carbon samples. Brunauer, Emmett, and Teller (BET) methods were applied to evaluate the specific surface area (m^2/g) of the samples (Table 1). These specific surface areas were used to determine the diffusion process through the porous material and selectivity for the catalyst reaction explained using the adsorption theory. The BET equation was used on the adsorption isotherms with P/P_0 values ranging from 0.05 to 0.3. The isothermal BET equation can be written as:

$$\frac{1}{W\left(\frac{P_0}{P}\right)-1} = \frac{1}{V_mC} + \left[\frac{C-1}{V_mC}\right]\frac{P}{P_0} \tag{6}$$

where W denotes the volume of absorbed gas at the relative pressure P/P_0, V_m is the volume of nitrogen gas that formed a monolayer at a solid

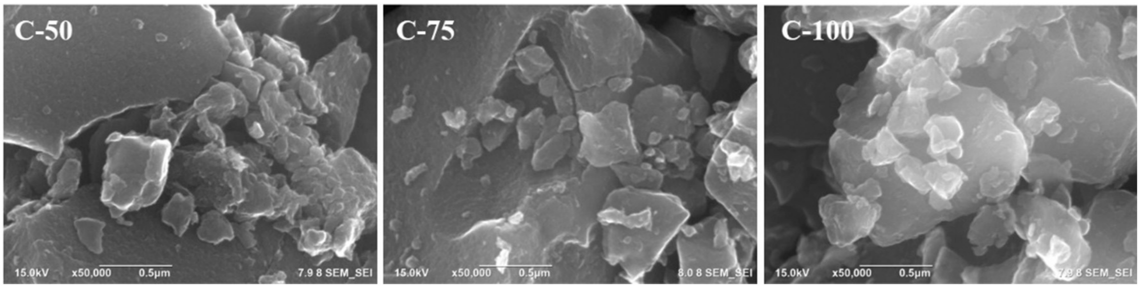

Fig. 1. Morphology of the activated carbon which is milled at different milling time.

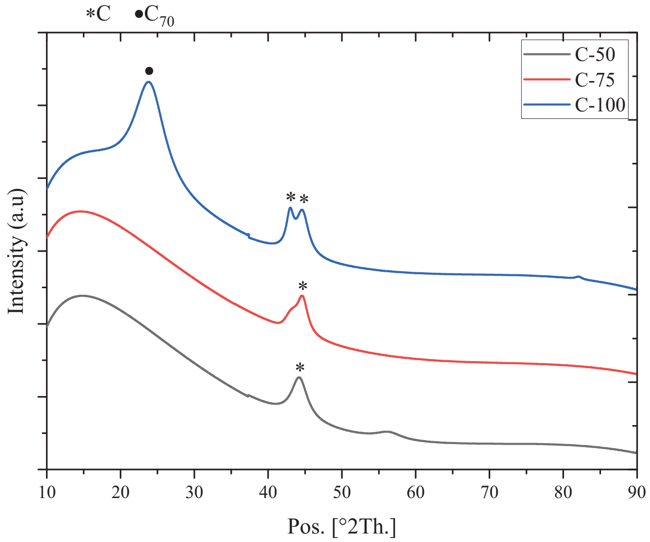

Fig. 2. XRD patterns of the as-prepared C-50, C-75, and C-100 samples with indicated carbon phases of * C and • C_{70}.

surface, P is the pressure of adsorption equilibrium, P_0 is the pressure of adsorption saturation and C is the constant of energy.

The values of V_m for all the samples were estimated from the slope (s) and intercepts (i) on the BET chart, achieving the specific surface areas of the produced activated carbon given by:

$$s = \frac{C-1}{V_m C} \tag{7}$$

$$i = \frac{1}{V_m C} \tag{8}$$

Combining Eqs. (7) and (8), one obtains:

$$V_m = \frac{1}{s+i} \tag{9}$$

The BET method was used to calculate the surface area of the sample (defined as the number of pores in each unit area of the sample). The specific surface area (S_{BET}) was estimated using:

$$S_{BET} = \frac{V_m N A_{cs}}{M} \tag{10}$$

where N is the Avogadro's number (6.023×10^{23} mol^{-1}), A_{cs} is the area of cross-section (16.2 Å) and M is the molecular weight (28.013 g/mol) of nitrogen.

Fig. 4 depicts the Barret Joyner Hallenda (BJH) pore size distribution - nitrogen adsorption at 77.35 K for C-50, C-75, and C-100 samples. Irrespective of the milling times, the pore radius distribution of the samples was in the range of 1 and 250 nm wherein the maximum peaks occurred at 1.53 (for C-50), 1.94 (for C-75), and 1.71 nm (for C-100). The average pore diameters of C-50, C-75, and C-100 samples were 3.06, 3.88, and 3.42 nm, respectively. According to the International Union of Pure Applied Chemistry (IUPAC) standard, the resulting pore diameters were classified as mesopores (pore diameter range of 2–50 nm). In addition, the pore volumes of C-50, C-75, and C-100 samples were 1.02 $\times 10^{-6}$, 6×10^{-8}, and 7.4×10^{-7} m^3/g, respectively.

Figs. 3 and 4 clearly revealed the activated carbon samples have a large specific surface area and excellent porosity. This porous morphology plays a significant role in the MW absorption, where a decrease in the pore diameter can appreciably increase the material's density or cavity concentration, thus leading to an alteration in the specific surface area responsible for the MW absorption. Consequently, an improvement in the specific surface area and porosity of the samples enables more interaction between carbon atoms and MW on the surfaces and interfaces.

3.4. Relative complex permeability and permittivity of the activated carbon

Fig. 5 displays the relative complex permeability and permittivity of C-50, C-75, and C-100 samples measured in the frequency range of 8.2–12.4 GHz. It is worth noting that the real permeability values of C-50, C-75, and C-100 samples were comparable due to their almost similar crystal phases. Conversely, the C-100 sample showed higher magnetic energy storage capacity (higher value of real permeability) than the C-50 and C-75 samples. Irrespective of the milling times, the real permeability values for all samples were gradually decreased to zero with the increase of MW frequency (Fig. 5(a)). The imaginary permeability of the C-100 sample (Fig. 5(b)) was related to magnetic loss which dropped significantly to almost zero in the range of 8.2 to 9 GHz and then fluctuated near zero. Meanwhile, the real permittivity of C-50 and C-75 samples (Fig. 5(c)) exhibited gradual declination trends with the increase in frequency. However, the real permittivity of the C-100 sample remained steady with the increase in frequency, indicating an excellent electrical field energy storage performance of C-100. The real permittivity (or dielectric constant) also determines how much the incoming energy can be reflected and absorbed by the proposed activated carbon. In the frequency range of 8.2 to 9.3 GHz, the imaginary permittivity (or dielectric loss factor) of C-100 sample was negative (Fig. 5(d)), indicating an electrical field energy storage in the material rather than dissipation. In addition, the electrical dipole polarization-enabled dielectric loss factor of the activated carbon specimen up to 9.3 GHz was mainly governed by the dominant heating mechanism or electrical field energy dissipation in the form of heat inside the material. It is important to note that the dielectric polarization not only depended on the strength of the applied electric field but also the geometry or crystal structure of the proposed activated carbon specimen.

3.5. Microwave reflection loss of activated carbon

Fig. 6 illustrates the MW absorption properties of all activated carbon

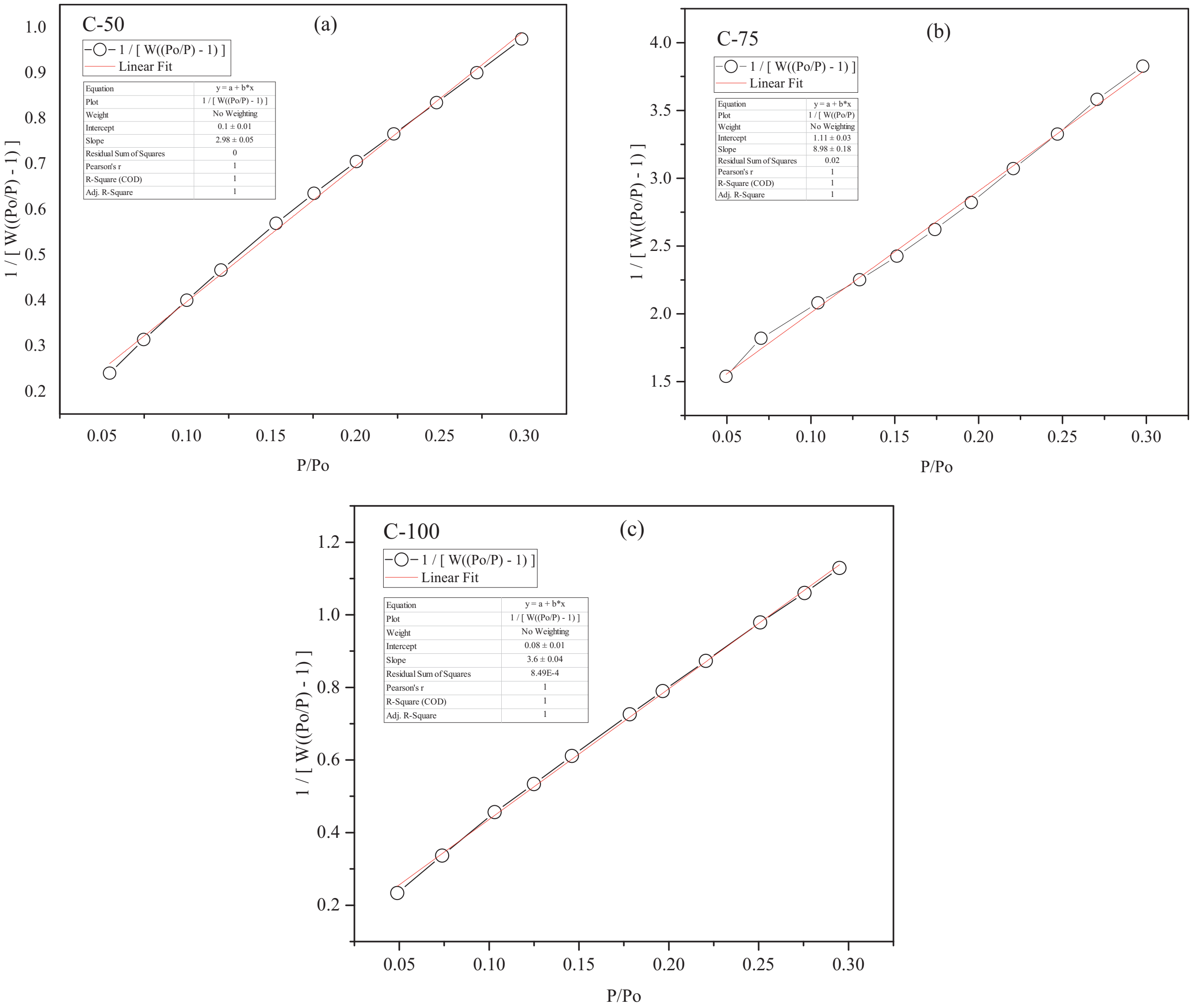

Fig. 3. Multi-point isothermal BET plot of all activated carbon specimens.

Table 1
The specific surface area of the activated carbons.

Sample code	Slope (s)	Intercepts (i)	The volume of nitrogen gas (V_m)	Specific surface area S_{BET} (m^2/g)
C-50	2.980	0.098	0.325	1131.617
C-75	8.984	1.109	0.099	345.102
C-100	3.605	0.075	0.272	946.499

specimens in terms of their frequency-dependent reflection loss (R_L). The R_L was found to be controlled by adjusting the milling time. The patterns of R_L for C-50 and C-75 were similar with an average value of approximately −10 dB. Conversely, the C-100 sample exhibited a prominent absorption band around 9 GHz with a bandwidth of 3 GHz. Interestingly, a mesoporous C-100 sample containing fullerene-C_{70} revealed significant MW absorbance in the X-band, indicating its potential for MW X-band applications in electronic devices. The produced fullerene-C_{70} dominated activated carbon also showed outstanding permeability and permittivity, suggesting its appropriateness for the MW X-band applications. Furthermore, the occurrence of a weak oscillation in the high-frequency range was attributed to the internal surface reflection within the mesopores. It was asserted that the milling process with optimal milling time could substantially enhance the microwave absorption capacity of the activated carbon. In short, the suggested fullerene-C70 enclosed activated carbon can lead to the development of

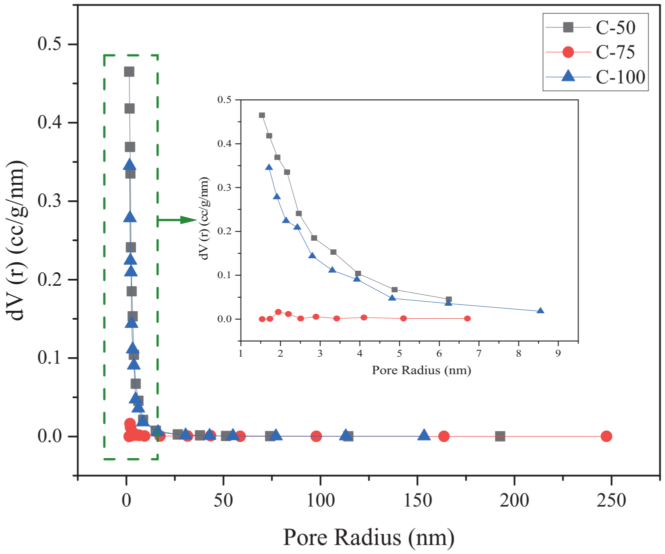

Fig. 4. BJH pore size distribution – nitrogen adsorption at 77.35 K for all activated carbon samples.

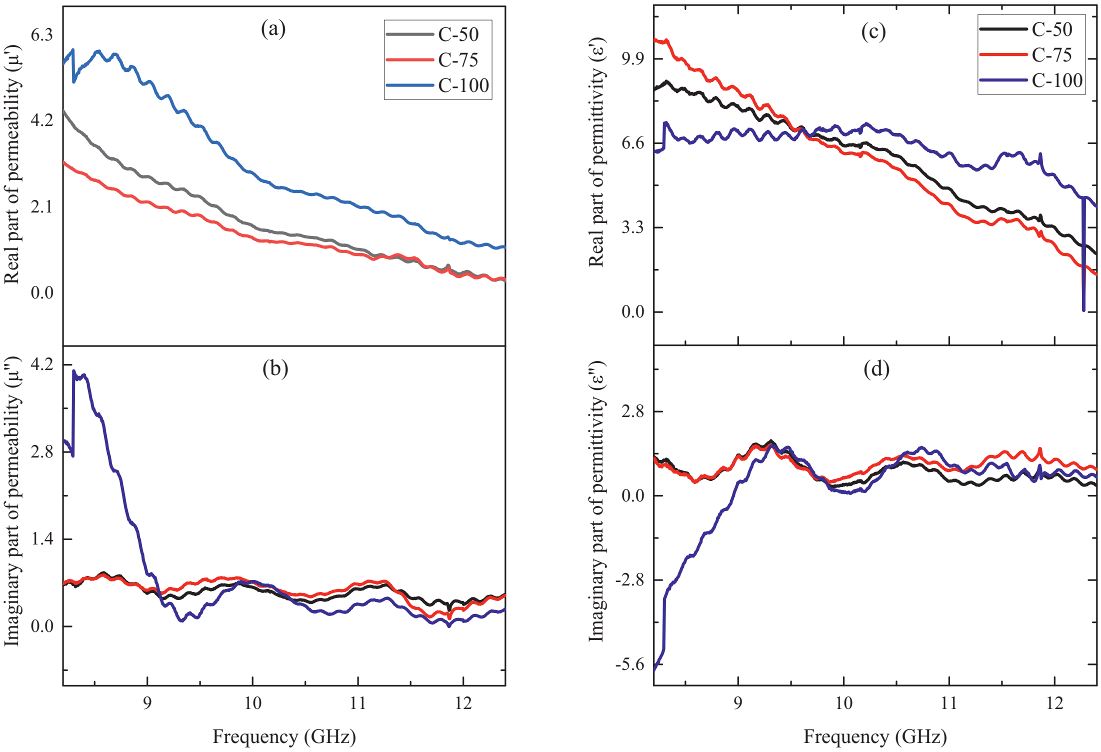

Fig. 5. MV frequency-dependent relative complex permeability and permittivity of 4 mm thick activated carbon.

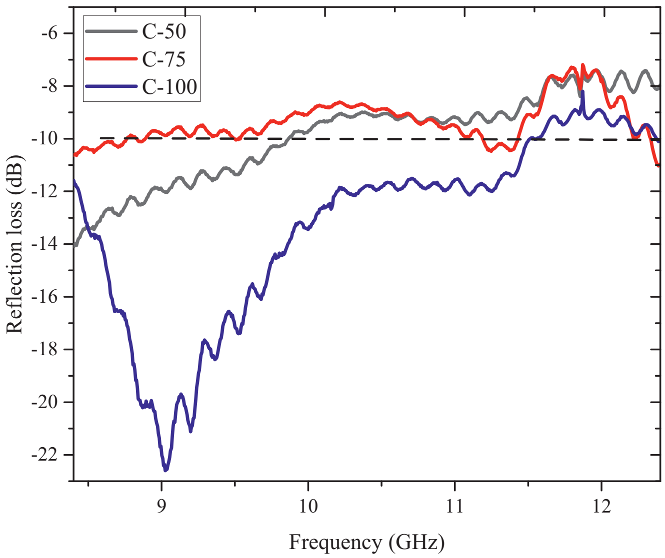

Fig. 6. MW reflection loss as a function of frequency for all activated carbon specimens of 4 mm thick.

low-cost, high-efficiency MW absorption materials desired for sundry applications.

4. Conclusions

For the first time novel activated carbon specimens (C-50, C-75, and C-100) were prepared from the coconut shells using a modified milling process plus a heating process. The milling times were varied (50, 75, and 100 min) to get mesoporous activated carbon with improved MW absorption properties. The surface morphology, phase, structure, surface area, porosity, and MW reflection loss of these samples were improved with the increase in milling times. Activated carbon obtained at a milling time of 100 min was the optimum one in terms of structures, morphology, and MW absorbance. The C-100 sample showed a phase transformation from cubic to the rhombohedral crystal structure (or fullerene-C_{70}). The specific surface area and mean pore diameter of the C-100 specimen were 946.499 m^2/g and 3.42 nm, respectively. The activated carbon-containing fullerene-C_{70} revealed excellent permeability and permittivity characteristics suitable for MW X-band applications. It was affirmed that by regulating the surface area and fullerene-C_{70} contents in the activated carbon the MW reflection loss can be tuned. The proposed fullerene-C_{70} based activated carbon can lead to the development of cheap and efficient MW absorption materials required for varied purposes.

Declaration of competing interest

The authors declare that they have no known competing financial interests or personal relationships that could have appeared to influence the work reported in this paper.

Acknowledgments

The authors are grateful to the Universitas Jenderal Soedirman Indonesia (Contract number: T/573/UN.23.18/PT.01.03/2021) and UTM Malaysia (UTMFR 20H65) for their financial assistance.

References

[1] H. Zhao, G. Zhang, R. MA, Synthesis and electromagnetic properties of nanocrystalline Ni-Zn Ferrite doped lanthanum, Nanotechnol. Precis. Eng. 8 (2010).

[2] C.-J. Li, B. Wang, J.-N. Wang, Magnetic and microwave absorbing properties of electrospun Ba(1–x)LaxFe12O19 nanofibers, J. Magn. Magn. Mater. 324 (2012) 1305–1311, https://doi.org/10.1016/j.jmmm.2011.11.016.

[3] B.K. Rai, S.R. Mishra, V.V. Nguyen, J.P. Liu, Synthesis and characterization of high coercivity rare-earth ion doped Sr0.9RE0.1Fe10Al2O19 (RE: Y, La, Ce, Pr, Nd, Sm, and Gd), J. Alloys Compd. 550 (2013) 198–203, https://doi.org/10.1016/j.jallcom.2012.09.021.

[4] W. Widanarto, E. Ardenti, S.K. Ghoshal, C. Kurniawan, M. Effendi, W.T. Cahyanto, Significant reduction of saturation magnetization and microwave-reflection loss in barium-natural ferrite via Nd3+ substitution, J. Magn. Magn. Mater. 456 (2018) 288–291, https://doi.org/10.1016/j.jmmm.2018.02.050.

[5] W. Widanarto, S. Khaeriyah, S.K. Ghoshal, C. Kurniawan, M. Effendi, W. T. Cahyanto, Selective microwave absorption in Nd3+ substituted barium ferrite composites, J. Rare Earths 37 (2019) 1320–1325, https://doi.org/10.1016/j.jre.2019.01.008.

[6] W. Widanarto, A.I. Ekaputra, M. Effendi, W.T. Cahyanto, S.K. Ghoshal, C. Kurniawan, E. Handoko, M. Alaydrus, Neodymium ions activated barium ferrite composites for microwave X-band absorber applications: synthesis and characterizations, Compos. Commun. 19 (2020) 51–55, https://doi.org/10.1016/j.coco.2020.02.008.

[7] W. Widanarto, M. Effendi, S.K. Ghoshal, C. Kurniawan, E. Handoko, M. Alaydrus, Bio-silica incorporated barium ferrite composites: evaluation of structure, morphology, magnetic and microwave absorption traits, Curr. Appl. Phys. 20 (2020) 638–642, https://doi.org/10.1016/j.cap.2020.02.019.

[8] N. Zhang, Y. Huang, M. Wang, X. Liu, M. Zong, Design and microwave absorption properties of thistle-like CoNi enveloped in dielectric Ag decorated graphene composites, J. Colloid Interface Sci. 534 (2019) 110–121, https://doi.org/10.1016/j.jcis.2018.09.016.

[9] H. Wei, X. Yin, X. Li, M. Li, X. Dang, L. Zhang, L. Cheng, Controllable synthesis of defective carbon nanotubes/Sc 2 Si 2 O 7 ceramic with adjustable dielectric properties for broadband high-performance microwave absorption, Carbon N. Y. 147 (2019) 276–283, https://doi.org/10.1016/j.carbon.2019.03.008.

[10] L. Liu, N. He, T. Wu, P. Hu, G. Tong, Co/C/Fe/C hierarchical flowers with strawberry-like surface as surface plasmon for enhanced permittivity, permeability, and microwave absorption properties, Chem. Eng. J. 355 (2019) 103–108, https://doi.org/10.1016/j.cej.2018.08.131.

[11] R. Pastore, A. Delfini, D. Micheli, A. Vricella, M. Marchetti, F. Santoni, F. Piergentili, Carbon foam electromagnetic mm-wave absorption in reverberation chamber, Carbon N. Y. 144 (2019) 63–71, https://doi.org/10.1016/j.carbon.2018.12.026.

[12] J. Ma, J. Shu, W. Cao, M. Zhang, X. Wang, J. Yuan, M. Cao, A green fabrication and variable temperature electromagnetic properties for thermal stable microwave absorption towards flower-like Co3O4@rGO/SiO2 composites, Compos. Part B Eng. 166 (2019) 187–195, https://doi.org/10.1016/j.compositesb.2018.11.119.

[13] J. Wang, W. Zhang, C. Zhang, Versatile fabrication of anisotropic and superhydrophobic aerogels for highly selective oil absorption, Carbon N. Y. 155 (2019) 16–24, https://doi.org/10.1016/j.carbon.2019.08.049.

[14] L. Wang, X. Yu, X. Li, J. Zhang, M. Wang, R. Che, Conductive-network enhanced microwave absorption performance from carbon coated defect-rich Fe 2 O 3 anchored on multi-wall carbon nanotubes, Carbon N. Y. 155 (2019) 298–308, https://doi.org/10.1016/j.carbon.2019.07.049.

[15] J. Luo, H. Zhang, Z. Zhang, J. Yu, Z. Yang, in: In-built Template Synthesis of Hierarchical Porous Carbon Microcubes From Biomass Toward Electrochemical Energy Storage 155, 2019, pp. 1–8, https://doi.org/10.1016/j.carbon.2019.08.044.

[16] Y. Wang, Q. Qu, S. Gao, G. Tang, K. Liu, Biomass derived carbon as binder-free electrode materials for supercapacitors, Carbon N. Y. 155 (2019) 706–726, https://doi.org/10.1016/j.carbon.2019.09.018.

[17] Y. Du, T. Liu, B. Yu, H. Gao, P. Xu, J. Wang, X. Wang, X. Han, The electromagnetic properties and microwave absorption of mesoporous carbon, Mater. Chem. Phys. 135 (2012) 884–891, https://doi.org/10.1016/j.matchemphys.2012.05.074.

[18] H. Zhao, Y. Cheng, W. Liu, L. Yang, B. Zhang, L.P. Wang, G. Ji, Z.J. Xu, Biomass-derived porous carbon-based nanostructures for microwave absorption, Nano-Micro Lett. 11 (2019) 1–17, https://doi.org/10.1007/s40820-019-0255-3.

[19] Z. Jia, C. Wang, A. Feng, P. Shi, C. Zhang, X. Liu, K. Wang, G. Wu, A low-dielectric decoration strategy to achieve absorption dominated electromagnetic shielding material, Compos. Part B Eng. 183 (2020), 107690, https://doi.org/10.1016/j.compositesb.2019.107690.

[20] D. Ding, Y. Wang, X. Li, R. Qiang, P. Xu, W. Chu, X. Han, Y. Du, Rational design of core-shell Co@C microspheres for high-performance microwave absorption, Carbon N. Y. 111 (2017) 722–732, https://doi.org/10.1016/j.carbon.2016.10.059.

[21] Y. Cheng, Z. Li, Y. Li, S. Dai, G. Ji, H. Zhao, J. Cao, Y. Du, Rationally regulating complex dielectric parameters of mesoporous carbon hollow spheres to carry out efficient microwave absorption, Carbon N. Y. 127 (2018) 643–652, https://doi.org/10.1016/j.carbon.2017.11.055.

[22] C. Zhou, S. Geng, X. Xu, T. Wang, L. Zhang, X. Tian, F. Yang, H. Yang, Y. Li, Lightweight hollow carbon nanospheres with tunable sizes towards enhancement in microwave absorption, Carbon N. Y. 108 (2016) 234–241, https://doi.org/10.1016/j.carbon.2016.07.015.

[23] S. Kumar, R. Chatterjee, Complex permittivity, permeability, magnetic and microwave absorbing properties of Bi3+ substituted U-type hexaferrite, J. Magn. Magn. Mater. 448 (2018) 88–93, https://doi.org/10.1016/j.jmmm.2017.06.123.

[24] K. Shi, J. Li, S. He, H. Bai, Y. Hong, Y. Wu, D. Jia, Z. Zhou, A superior microwave absorption material: Ni2+-Zr4+ Co-doped barium ferrite ceramics with large reflection loss and broad bandwidth, Curr. Appl. Phys. 19 (2019) 842–848, https://doi.org/10.1016/j.cap.2019.03.018.

[25] P. Meng, K. Xiong, L. Wang, S. Li, Y. Cheng, G. Xu, Tunable complex permeability and enhanced microwave absorption properties of BaNixCo1-xTiFe10O19, J. Alloys Compd. 628 (2015) 75–80, https://doi.org/10.1016/j.jallcom.2014.10.163.

[26] E. Handoko, I. Sugihartono, S. Budi, M. Randa, Z. Jalil, M. Alaydrus, The effect of thickness on microwave absorbing properties of barium ferrite powder, J. Phys. Conf. Ser. 1080 (2018), https://doi.org/10.1088/1742-6596/1080/1/012002.

[27] S. Jeon, J.Y. Jang, J.R. Youn, J.H. Jeong, H. Brenner, Y.S. Song, Fullerene embedded shape memory nanolens array, Sci. Rep. 3 (2013) 1–6, https://doi.org/10.1038/srep03269.

[28] J. Zhong, K. Jia, Z. Pu, X. Liu, Sandwich-like graphite-fullerene composites with enhanced electromagnetic wave absorption, J. Electron. Mater. 45 (2016) 5921–5927, https://doi.org/10.1007/s11664-016-4800-2.